Electrochimica Acta 91 (2013) 20–29

Contents lists available at SciVerse ScienceDirect

Electrochimica Acta

journal homepage: www.elsevier.com/locate/electacta

Improved kinetics from ion advection through overlapping electric double layers in nano-porous electrodes

Isaac B. Sprague, Prashanta Dutta*

School of Mechanical and Materials Engineering, Washington State University, Pullman, WA 99164-2920, USA

ARTICLE INFO

Article history:
Received 22 October 2012
Received in revised form
29 November 2012
Accepted 5 December 2012
Available online 27 December 2012

Keywords:
Electric double layer
Electrode kinetics
Nano-pore
Electrolyte advection

ABSTRACT

A novel device architecture is presented for laminar flow fuel cell by introducing an ion advection flux within the electric double layer (EDL). Typically advection in the EDL is negligible because the near wall electrolyte velocity is zero. However, by using nano-pores, a non-negligible ion advection flux can be developed in the charged regions of the EDL. In this article we study how advection in the EDL affects the kinetic performance of electrochemical cells. To accomplish this we use a laminar flow fuel cell model based on the Poisson–Nernst–Planck and Frumkin–Butler–Volmer equations. The model contains nonlinear physics with very disparate length scales due to the complex 3-dimensional nature of the nano-porous device. To account for these difficulties, the full mathematical model is solved numerically using a novel numerical algorithm developed based on domain decomposition method. The presented algorithm allows the simulation of complex near wall electrode effects, such as overlapping double layers in a nano-pore, in the context of a complete device, which would have been numerically prohibitive otherwise. The presence of an advection flux through nano-pores on the order of the EDL width yields some novel phenomena that affect the structure of electrode–electrolyte interface. The most surprising result is the development of a region of zero charge at the electrodes in the upstream regions of longer nano-pores. We also show that electrolyte advection within the EDL can be used to enhance the kinetic performance of electrodes in electrochemical cells.

1. Introduction

In galvanic (i.e. power-producing) cells, such as fuel cells, the rate at which electrode reactions are able to proceed greatly impacts the electrical power produced by the cell. Many factors impact the rate of the electrode kinetics such as catalyst composition, reactant transport, flow rate, active area, as well as the interface structure between the electrode and electrolyte, or the electric double layer (EDL). As microfabrication and nano-patterning techniques improve, the opportunity arises to affect the EDL, and therefore increase kinetic performance through the electrode microstructure. One possible way to attain this performance increase is the introduction of an advection ion flux in the charged regions of the EDL through the use of nano-pores, which is the focus of this work.

Recently, there have been several studies investigating the role of the fundamental relationship between the EDL and electrode kinetics [1–5] including the impact of the electrolyte on the diffuse layer portion of the EDL [6,7]. The nature of electrolytes in porous media, such as the time evolution of the EDL charging process, has also been studied [8]. Recent investigations have focused on novel diffuse region behavior resulting from channel/electrode structures whose sizes are on the same order as the EDL width. For example, cylindrical electrodes with diameters on the nano-scale exhibit greatly altered electrode kinetics [9], and nano-pores in planar electrodes have been found to affect the EDL structure [10], and can lead to fully depleted electrolyte regions [11]. The depletion or enrichment of electrolyte at the junctions of nano- and micro-scale channels (known as concentration polarization) has attracted much attention [12,13] and can impact ionic currents in electrochemical cells [14,15].

The effects of electrode geometry on electrode kinetics are well studied. Porous electrodes are often used to improve kinetic performance because they provide increased effective electrode surface area for more current to be generated per unit volume. Also flow of reactant streams through the pores greatly improves reactant transport. Recently, the effect of pores with nanometer scale dimensions on the EDL and electrode kinetics has been considered [16–18]. Nano-pores can alter electrode kinetics due to their small scale allowing for overlapping double layers altering the electrode–electrolyte interface. Nano-pores also provide a second interesting opportunity that has not been studied previously in fuel cell platform. The flow of an electrolyte through a nano-pore introduces an advection flux within the electrode–electrolyte interface

* Corresponding author. Tel.: +1 509 335 7989; fax: +1 509 335 4662.
E-mail address: dutta@mail.wsu.edu (P. Dutta).

0013-4686/$ – see front matter © 2012 Elsevier Ltd. All rights reserved.
http://dx.doi.org/10.1016/j.electacta.2012.12.015

as the characteristic dimension for flow approaches that of the EDL [19,20], and this can be used to improve the kinetic performance in fuel cell.

The goal of this work is to introduce an electrode design where the kinetic performance can be influenced by electrolyte advection. We present a laminar flow fuel cell [21–23] device architecture similar to Kjeang et al. [24] where fuel and oxidant reactant streams are fed through opposing porous electrodes into a central microchannel where they then exit to waste. However, in this work we consider a nano-porous electrode with regular pore spacing and structure. The electrolyte stream flows normally through the electrode. This allows for the electrolyte advection to provide performance benefits at the nano-scale EDL [19,20] as well as the transport benefits seen at the macro-scale in Kjeang's et al. work. The performance of the new electrode design is studied within the context of a complete device.

2. Device configuration

The device is configured so the fuel and oxidant inlets are on opposing sides of a planar microchannel. The fuel and oxidant electrolyte streams flow from their corresponding upstream inlets through the porous anode and cathode, respectively. Finally, the two electrolyte streams converge in the center region of the planar channel (i.e. the region separating the electrodes) and are sent to waste through an outlet in the ceiling, as shown in Fig. 1.

To limit the complexity of the device analysis, the nano-pores are considered to be slots (i.e. the pore width $\ll$ pore height) allowing for a 2-dimensional simulation in the electrode regions. The anode and cathode electrodes are separated by a distance d_4 in the planar microchannel of height d_1 and width d_2. Each electrode has a stream-wise dimension of d_3. The nano-pores are assumed to extend the full height of the electrode and are regularly spaced along the electrode. The nano-pores have a width of d_5 and a spacing of d_6 as shown in the inset of Fig. 1.

For the bulk electrolyte advection through the pores to influence the electrode performance, the physical values of the dimensions d_5 and d_6 must be on the order of the Debye length. The remaining dimensions d_1, d_2, d_3, d_4 are consistent with typical planar microchannel length scales. Table 1 summarizes the intended order of magnitude for the typical values of the dimensions.

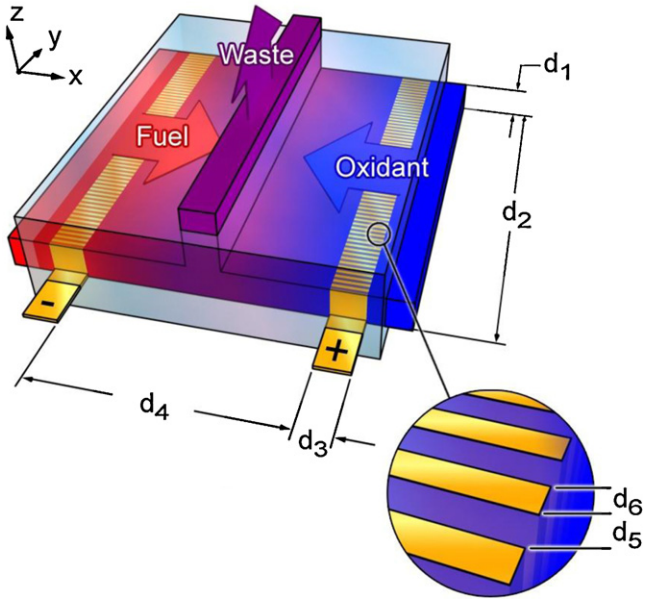

Fig. 1. Device configuration used for electrolyte advection through nano-porous electrodes. The device is comprised of two inlets on opposing sides of a microchannel that feed to porous electrodes which are separated by a central region. The nano-pores (inset) are considered to be slots extending the full height of the planar channel.

Table 1
Intended order of magnitude for key dimensions in porous electrode device.

d_1	d_2	d_3	d_4	d_5	d_6
10 μm	1 cm	1 μm	100 μm	10 nm	10 nm

To focus the study on the nano-porous electrode, generic fuel cell chemistry is used. The general overall device reaction can be written as:

$$Fuel + Oxidant \rightarrow Waste \tag{1}$$

The overall reaction is split into separate half reactions so that the exchange of electrons can be harnessed as electrical work. The two half reactions are therefore:

$$Fuel \underset{k'}{\overset{k}{\leftrightarrow}} S_{C^+} \cdot C^+ + n \cdot e^- + Waste \tag{2a}$$

for fuel oxidation and

$$S_{C^+} \cdot C^+ + n \cdot e^- + Oxidant \underset{k}{\overset{k'}{\leftrightarrow}} Waste \tag{2b}$$

for oxidant reduction. Here n is the number of electrons (e^-) liberated per mole of fuel. The term S_{C^+} is the stoichiometric coefficient for the cation (C^+). Each half reaction is allowed to proceed in either direction as determined by the forward and reverse rate constants k and k', respectively.

In this study, the primary interest is the effect of the bulk electrolyte advection on ion transport and how this affects the electric double layer and electrode kinetics. Therefore, we assume that the neutral reactants of fuel and oxidant are present in excess and we do not consider their influence on electrode kinetics. Also, to maintain simplicity in this investigation we consider a simple binary electrolyte consisting of a cation (C^+) and an anion (A^-) of unit charge, $z_+ = -z_- = 1$. In Eq. (2) we have taken the cation as the working ion, being produced by fuel oxidation and consumed by oxidant reduction. The anion is inert and does not participate in the electrode reactions.

3. Mathematical model

3.1. Governing equations

The continuum quantities of anion and cation concentrations (c_-, c_+) and potential (ϕ) in the electrolyte phase are described by the Poisson–Nernst–Planck equations.

$$\nabla \cdot \vec{N}_i^* = 0 \tag{3}$$

$$-\nabla \cdot (\varepsilon \nabla \phi) = F \sum z_i c_i \tag{4}$$

where $\vec{N}_i^*$ is the ionic current density, F is the Faraday constant, ε is the permittivity of the electrolyte, and z_i is the charge of the ith ion ($i = +, -$). The net ionic flux density is given by the sum of the advection, diffusion, and migration flux densities:

$$\vec{N}_i^* = \vec{v} c_i - D_i \nabla c_i - z_i \omega_i F c_i \nabla \phi \tag{5}$$

where $\vec{v}$ is the electrolyte velocity, D is the diffusion coefficient, and ω is the ionic mobility. The bulk flow of the electrolyte stream is given by the incompressible steady-state Navier–Stokes and continuity equations:

$$\nabla \cdot (\rho_v \vec{v}\vec{v}) = \nabla \cdot (\mu_v \nabla \vec{v}) - \nabla p - F \nabla \phi \sum z_i c_i \tag{6}$$

$$\nabla \cdot (\rho_v \vec{v}) = 0 \tag{7}$$

where ρ_v and μ_v are the fluid density and viscosity, and p is the pressure. Finally, the rate at which the half reactions proceed is determined by the generalized-Frumkin–Butler–Volmer equation:

$$j = Fn\left[k \cdot exp\left(\frac{(1-\beta)z_+F}{RT}\Delta\phi_S\right) - k'c^+ exp\left(-\frac{\beta z_+F}{RT}\Delta\phi_S\right)\right] \tag{8}$$

where j is the current density; $\Delta\phi_S$ is the change in potential between the electrode and reaction plane (i.e. across the Stern layer), $\Delta\phi_S = \psi_{El} - \phi_{RP}$; and R and T are the ideal gas constant and absolute temperature. β is the kinetic symmetry factor and is assumed to be 0.5.

It is worth mentioning here that fuel cells are power-producing electrochemical cells and therefore the electrode reactions are exothermic (i.e. they proceed spontaneously in the presence of a catalyst). As the reactions proceed, a charge builds up in the electrodes because of the exchange of electrons with the reactants. The resulting electrode potential serves to slow the reaction rate so that electrode reactions proceed in equilibrium with the flow of electrons that can be routed through the external electronic circuit. In Eq. (8), $\Delta\phi_S = 0$ corresponds to the electrode reactions in the absence of an electrode charge and they proceed at their thermodynamic spontaneous rate as determined by the rate constants. Generally, this is the fastest electrode kinetics that can proceed in a fuel cell.

3.2. Normalization scheme

Since the focus of this work is an investigation into the effect of electrolyte advection through a nano-pore on device performance, it is preferable to normalize the system of equations (Eqs. (3)–(8)). Here dimensionless variables are introduced for concentration ($C_i = c_i/c_{in}$), electrolyte potential ($\Phi = \phi z_+F/RT$), and velocity ($\vec{V} = \vec{v}d_1/D_+$). The spatial coordinates are also scaled by the channel height yielding $X = x/d_1$, $Y = y/d_1$, and $Z = z/d_1$. The dimensionless Nernst–Planck equation for ionic transport can now be written:

$$\nabla \cdot (\vec{V}C_i - \nabla C_i - C_i\nabla\Phi) = 0 \tag{9}$$

as well as the dimensionless Poisson's equation:

$$-\in_D^2 \nabla^2\Phi = C_+ - C_- \tag{10}$$

where λ_D is the Debye length and $\in_D = \lambda_D/d_3$ is the relative Debye length. To write the dimensionless Navier–Stokes and continuity equations, the dimensionless variables for pressure ($P = pd_1^2/\mu_v D_+$) is introduced. The dimensionless Navier–Stokes and continuity equations become:

$$\frac{1}{Sc}\nabla \cdot (\vec{V}\vec{V}) = \nabla^2\vec{V} - \nabla P - \Gamma(C_+ - C_-)\nabla\Phi \tag{11}$$

$$\nabla \cdot \vec{V} = 0 \tag{12}$$

where Sc is the Schmidt's number ($Sc = \mu_v/\rho_v D_+$) and Γ is a dimensionless electrostatic body force number ($\Gamma = \mu_v\omega_+/d_1^2 D_+$). Finally, the dimensionless generalized-Frumkin–Butler–Volmer equation can be written with the introduction of the dimensionless current ($J = jd_1/4nFD_+c_{in}$) and dimensionless rate constants; $K = kd_1/4D_+c_{in}$ and $K' = k'd_1/4D_+$:

$$J = K \cdot \exp((1-\beta)\Delta\Phi_S) - K'C_+ \exp(-\beta\Delta\Phi_S) \tag{13}$$

3.3. Device boundary conditions

For the proposed microfluidic fuel cell, the device boundary consists of two inlet reservoirs for the fuel and oxidant and one outlet reservoir for waste, channel walls, and the electrode regions. The boundary conditions for the inlets and outlets are derived from the condition that no current may go in or out of the device. In fuel cells, current only flows in a closed loop between the anode and cathode electrodes which are connected via the electrolyte and electronic circuit (not depicted). Hence, there can be no current within the electrolyte at the inlet or outlet reservoirs. Also, owing to the large size of reservoirs compared to the nanochannel in the electrode region, there are no gradients in electrolyte potential or concentration in the inlet and outlet reservoirs. For the electrode–electrolyte interface, we assume that the continuum fields extend up to the reaction plane (interface between the diffuse layer and Stern layer portions of the electric double layer). At the reaction plane, the ionic flux can be related to the electrode current. For electrolyte potential, an adaptation of the Stern model for the electric double layer is used as the boundary condition. Finally, for fluid flow no-slip and no-penetration conditions is imposed along the device walls, a known flow velocity at the inlets and an outflow boundary condition at the outlet. A complete summary of the device boundary conditions is shown in Table 2.

Table 2
Device boundary conditions.

Continuum field	Inlet	Electrode	Wall	Outlet
Φ	$\frac{\partial\Phi}{\partial X} = 0$	$\Delta\Phi_S = \in_D\delta\frac{\partial\Phi}{\partial n}\Big\vert_{Reaction\ Plane}$	$\frac{\partial\Phi}{\partial n} = 0$	$\frac{\partial\Phi}{\partial Z} = 0$
C_+	$\frac{\partial C_+}{\partial X} = 0$	$\vec{N}_+ \cdot \vec{n} = 4J$	$\vec{N}_+ \cdot \vec{n} = 0$	$\frac{\partial C_+}{\partial Z} = 0$
C_-	$\frac{\partial C_-}{\partial X} = 0$	$\vec{N}_- \cdot \vec{n} = 0$	$\vec{N}_- \cdot \vec{n} = 0$	$\frac{\partial C_-}{\partial Z} = 0$
$\vec{V}$	$\vec{V} \cdot \vec{n} = V_{in}$	$\vec{V} = 0$	$\vec{V} = 0$	$P = 0$

Here $\vec{n}$ is the outward pointing boundary normal, and δ is the ratio of Stern layer to Debye layer thickness, λ_S/λ_D.

4. Computational domains

The device design presented in Section 2 (Fig. 1) consists of a complex multidimensional domain with very disparate length scales (i.e. nanometer size pore, micron scale channel width and height, and meso size device length). Thus, direct solution of the full domain would not be possible, even numerically. Therefore, in order to proceed we divide the domain into 3 regions in a way that is analogous to the domain decomposition used elsewhere to obtain analytic approximations of the singular perturbation problem through asymptotic analysis [5]. The regions are inner regions for the anode and cathode electrodes which are connected via an outer region for the electrolyte between the electrodes. The inner regions are focused on the nano-scale interfacial effects between the electrode and electrolyte, while the outer region provides the micro-scale link between the anode and cathode. The individual regions are much simpler to analyze than the full domain. To ensure that the composite solution from the separate regions yields the correct device description we require that the continuum fields (C_i, Φ, $\vec{V}$, P) and their derivatives are continuous across the interfaces between the outer region and the inner regions:

$$C_{i,inner}(X,Y,Z)|_{int} = C_{i,outer}(X,Y,Z)|_{int} \tag{14a}$$

$$\frac{\partial C_{i,inner}}{\partial X}(X,Y,Z)\Big|_{int} = \frac{\partial C_{i,outer}}{\partial X}(X,Y,Z)\Big|_{int} \tag{14b}$$

$$\Phi_{inner}(X,Y,Z)\Big|_{int} = \Phi_{outer}(X,Y,Z)\Big|_{int} \tag{14c}$$

$$\frac{\partial\Phi_{inner}}{\partial X}(X,Y,Z)\Big|_{int} = \frac{\partial\Phi_{outer}}{\partial X}(X,Y,Z)\Big|_{int} \tag{14d}$$

where the subscripts *inner* and *outer* specify which region the continuum variable is from and *int* refers to values at the interface boundary in that region.

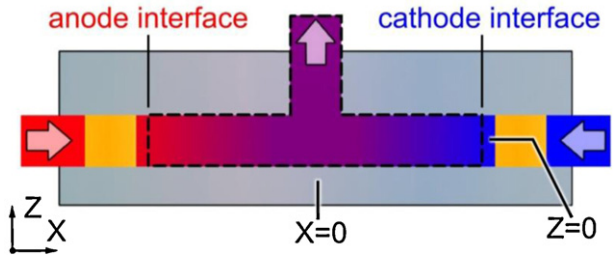

Fig. 2. Computational domain for the outer bulk electrolyte region. The domain is 2 dimensional in the *X*–*Z* plane and extends from just inside the anode electrode to just inside the cathode electrode and includes the device outlet.

The outer region resolves the bulk electrolyte region that resides between the anode and cathode electrodes. Here, we assume that the continuum fields (C_i, Φ, $\vec{V}$, P) are not significant functions of Y (i.e. $\partial/\partial Y = 0$) because the width d_2 of the channel is significantly greater than the channel height d_1. Therefore, the outer region can be considered as 2 dimensional in the *X*–*Z* plane. This further simplifies the computational domain of the bulk region which is shown as the dashed line in Fig. 2 and spans from the anode interface to the cathode interface and includes the outlet.

The inner regions resolve the electrolyte–electrode interface for the anode and cathode. The porous electrodes have a regular pore structure and span the full width and height of the channel. All pores along an electrode have constant interface and inlet conditions, therefore the pores can be assumed to be periodic along the electrode and only a single pore needs to be considered. This is justified through our assumption in the outer region that the continuum fields (C_i, Φ, $\vec{V}$, P) are not significant functions of Y and a similar argument can be constructed for the upstream inlets of each electrode. The computational domains are shown in Fig. 3 for the anode (Fig. 3a) and cathode (Fig. 3b).

In Fig. 3 we have considered the inner regions to be 2 dimensional in the *X*–*Y* plane. This can be done because the characteristic dimension in the nano-pore is the pore width d_5 and the continuum fields (C_i, Φ, $\vec{V}$, P) are, therefore, not significant functions of Z (i.e. $\partial/\partial Z = 0$). The inlet and interface boundaries are taken to be far away from the electrode surface relative to the diffuse layer thickness (i.e. $\lambda_D/\Delta x_{inl} \sim \lambda_D/\Delta x_{\text{int}} \to 0$). In this way the boundaries can be assumed to be in the electrically neutral bulk electrolyte.

The scaling arguments used to reduce the computational domains also reduce the continuity conditions across the interfaces. The continuity conditions are now:

$$C_{i,inner}(X)|_{int} = C_{i,outer}(X)|_{int} \tag{15a}$$

$$\left.\frac{\partial C_{i,inner}}{\partial X}(X)\right|_{int} = \left.\frac{\partial C_{i,outer}}{\partial X}(X)\right|_{int} \tag{15b}$$

$$\Phi_{inner}(X)\big|_{int} = \Phi_{outer}(X)\big|_{int} \tag{15c}$$

$$\left.\frac{\partial \Phi_{inner}}{\partial X}(X)\right|_{int} = \left.\frac{\partial \Phi_{outer}}{\partial X}(X)\right|_{int} \tag{15d}$$

because the continuum fields (C_i, Φ, $\vec{V}$, P) are considered not to be significant functions of Y or Z at the region interfaces.

5. Numerical technique

The full PNP-NS model (Eqs. (9)–(12)) is not trivial to solve in each region, even numerically. The difficulty arises from the highly coupled and nonlinear nature of the system of equations and boundary conditions. Furthermore, the 2-dimensional geometry considered in each domain prevents the use of existing analytical solutions. A numerical scheme is necessary to solve the equations across the 2-dimensional domains with the complex boundary conditions developed in the previous sections. An in-house numerical model is developed to simulate the PNP-NS-gFBV model in each domain. The spatial resolution used for the numerical discretization was 0.5 μm in the outer region and 0.1–0.05 nm in the inner regions. The details of the numerical scheme are presented elsewhere [3]. Our numerical model uses an iterative scheme until a convergence criterion is met. For this study, the convergence criterion was that the relative difference in the anode and cathode current densities as well as the relative change in the interfacial values for the final iteration be less than a specified tolerance. Briefly, the steps of the algorithm are: first the cathode inner region is solved using the guess values of the interface quantities, then the flux densities and ionic current across the cathode interface are calculated and used in the solution of the outer region continuum variables. The cathode interface quantities are then updated based on the outer region distributions. Next, the same is done for the anode and the full set of steps is iterated until convergence. Upon convergence, the continuum fields satisfy the interfacial continuity conditions in Eq. (15). Using four 3.33 GHz cores with shared 6 GB memory, convergence took between 4 and 24 h depending on model inputs. The continuity of the continuum field distributions is shown in Fig. 4 for the anode and cathode.

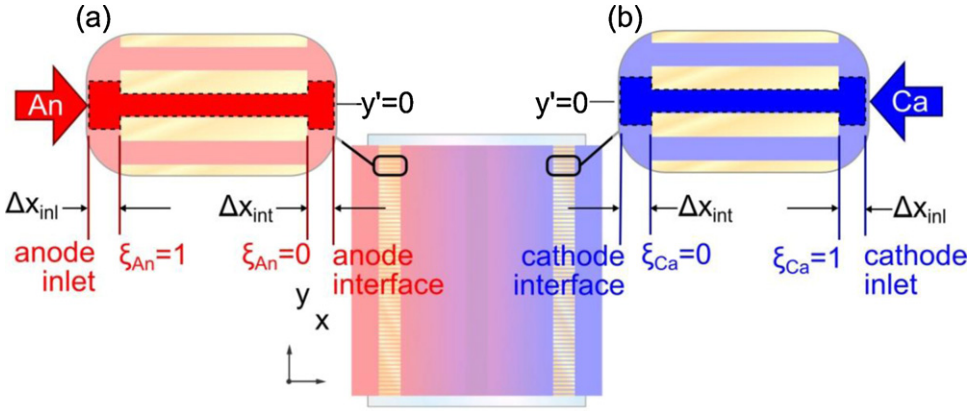

Fig. 3. Computational domains for the (a) anode and (b) cathode inner regions. Only a single pore is considered in each region due to the periodic nature of the regular nano-pore structure. The computational domain is 2 dimensional in the *X*–*Y* plane and includes the full pore with the upstream inlet and downstream interface boundaries extending far enough from the electrode to be in the bulk electrolyte. The inner coordinate system consists of y' and a rescaled inner coordinate, $\xi = (\pm x - d_4/2)d_3$.

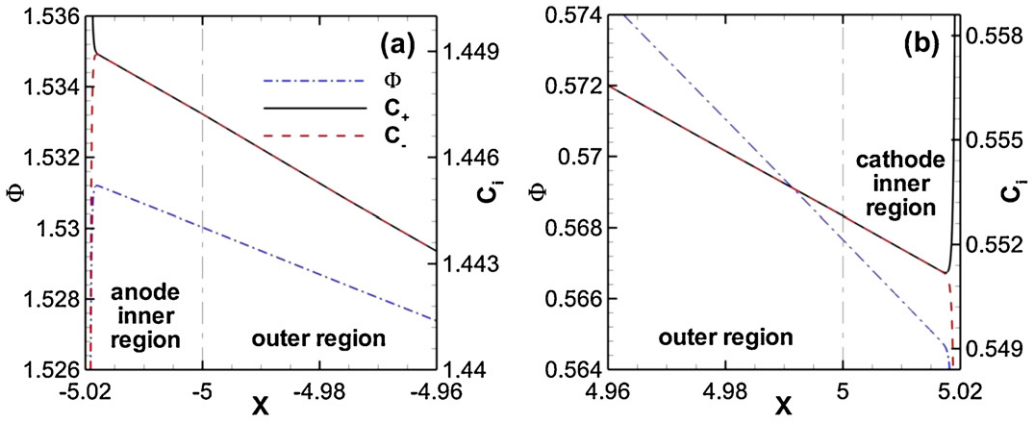

Fig. 4. Continuum distributions across the interfaces at the anode and cathode. The continuum fields are continuous across the interfaces located at $X = \pm 5$.

6. Results and discussion

The key device parameters analyzed in this study are the pore relative length, $\alpha = d_3/d_5$, the average fluid velocity along the pore axis, $V_{avg} = V_{in}/\theta$, and the relative pore diameter, $\gamma = d_5/\lambda_D$ Additional device parameters (ratio of the electric double layer widths, $\delta = \lambda_S/\lambda_D$, and the electrode porosity, $\theta = d_5/(d_6 + d_5)$) were also studied (not shown) but they did not appreciably influence the device in an interesting manner. Therefore, for the results presented, they were held constant at $\theta = 0.5, \delta = 0.1$. The following parameters were also held constant throughout: $d_1/d_4 = 0.1$, $\in_D = 2 \times 10^{-4}$, $Sc = 107$, $\Gamma = 4040$, $K_{An} = K'_{Ca} = 1 \times 10^{-4}$, and $K'_{An} = K_{Ca} = 1 \times 10^{-9}$

The entire operating range of the fuel cell is considered from short circuit to open circuit. The inputs to the model are the electrode potentials, and the model output is the current density. The anode electrode potential (Ψ_{An}) is specified as zero, while the cathode electrode potential (Ψ_{Ca}) is increased incrementally from zero until the total cathode current density, J_{Ca}, equals zero, which corresponds to the open circuit load. The average electrode current density is calculated by the surface integral of the local current density as:

$$J_{El} = \frac{1}{A}\int_S J_{El,local}\, dS \tag{16}$$

where A is the electrode surface area. It is worth mentioning that when considering porous electrodes there are two different electrode surface areas that can be considered. Commonly the surface area used is the nominal plane of the electrode ($A = d_1 \cdot d_2$) and porosity is accounted for through an additional parameter that represents the electrochemically active area of electrode. This current density will be referred to as J_{cell}. For this study, we also use the actual surface area ($2A[1 + \theta(\alpha - 1)]$) to study performance changes that are due to the electrolyte advection effect only, and this current density will be referred to as J_{pore}. The device current density is related to the electrode current densities by:

$$J_{pore} = J_{pore,An} = -J_{pore,Ca} \tag{17a}$$

and the pore and cell power density can be calculated as

$$PD_{pore} = J_{pore} \cdot \Psi_{pore} \tag{17b}$$

$$PD_{cell} = J_{cell} \cdot \Psi_{pore} \tag{17c}$$

We include the two different current and power densities for the following reasons. The cell power density is the standard for devices with porous electrodes. However, changes in pore geometry alone will significantly affect this performance metric. To isolate the performance improvement from the electric double layer advection affect we also include the pore power density which is independent of pore geometric affects.

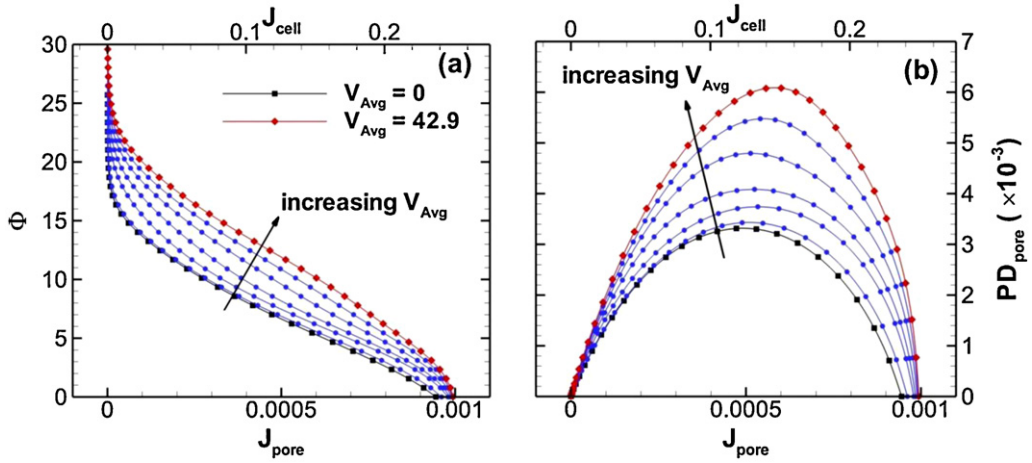

Fig. 5. Device performance for various average pore velocities, V_{Avg}. Performance plots shown are (a) a *V–I* plot and (b) a power density plot. The average pore velocities used are: 0, 0.43, 4.29, 10.7, 21.5, 32.2, and 42.9. The remaining parameters are ($\alpha = 500$, $\gamma = 1$).

6.1. Electrolyte advection effect on performance

The performance plots in Fig. 5 reveal the strong potential benefits from electrolyte advection through a nano-pore for a fuel cell electrode. Not surprisingly, the short circuit current is not significantly improved in Fig. 5a with increasing average pore velocity. This is likely due to the fact that at short circuit the electric double layers at the electrodes are at or near the point of zero charge, meaning there is little charged diffuse layer for the advection flux to act on. The benefit from the electrolyte advection through a nano-pore is seen in the power-producing range of the fuel cell, at potentials away from short or open circuit. Fig. 5b shows that the peak power is roughly doubled with an average pore electrolyte velocity of 42.9 over a device with no flow.

The distributions of electrolyte potential, cation concentration, and anion concentration along the cross device axis are shown in Fig. 6. The results are shown for the 3 regions: anode inner (left panel), bulk fluid (center panel), and cathode inner (right panel). In the inner regions, the distributions are taken at the centerline of the typical periodic pore and are presented against the rescaled inner X spatial coordinate, $\xi = (\pm x - d_4/2)/d_3$. In the outer region, the distributions are taken at $Z = 0$.

The electrolyte potential distribution in Fig. 6a shows the development of electrolyte potential gradient along the pore axis. This is most visible in the anode pore. The potential gradient is a result of the advection flux in a region of the electrolyte with a net nonzero charge density. The nonzero charge density is a result of balancing the net charge density developed in the polarized electrode. This leads to an excess of cations in the anode, where the electrode has a negative charge. The difference in cation and anion concentrations in the anode nano-pore is visible through comparison of Fig. 6b and c. The advection flux for cations is, therefore, much greater than the advection flux of anions. However, the net difference in cation and anion flux densities must be equal to the net ionic current density as discussed earlier. Therefore, a potential gradient as well as a cation concentration gradient must develop to retard the flow of cations along the pore through migration and diffusion.

Another interesting phenomenon is the increasingly nonlinear anion distribution along the pore with increasing fluid velocity, again most visible in the anode. The anion flux must remain constant along the pore axis. However, at the exit of the pore there is a steep potential gradient as the electrolyte transitions to its bulk state. This gradient yields a much higher migration flux. Therefore, to maintain a constant flux the concentration of anions is depleted, lessening the advection flux. Farther upstream in the pore the electric field is significantly less so the concentration increases, again allowing the advection flux to be dominant. Similar phenomena are occurring at the cathode pore as well but due to the scale in Fig. 6 the distributions are difficult to visualize.

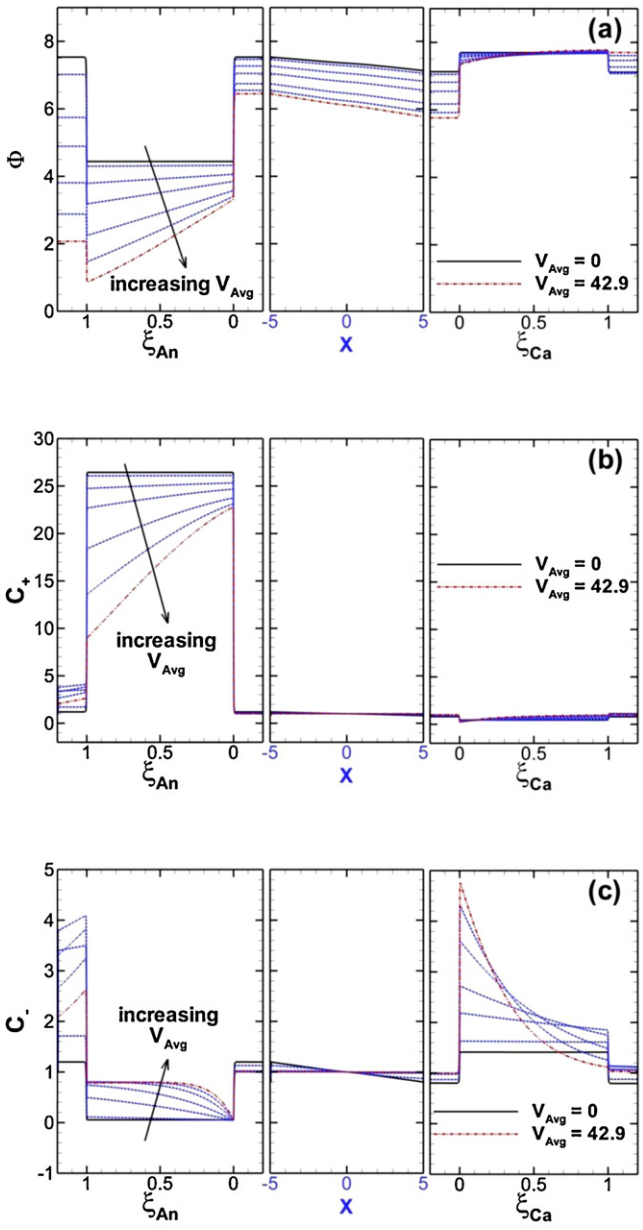

Fig. 6. Electrolyte potential and concentration distributions along pore for various average pore velocities, V_{Avg}. The (a) electrolyte potential, (b) cation concentration, and (c) anion concentration distributions are taken along the centerline of the computational domains and are shown for $\Psi_{An} = 0$, $\Psi_{Ca} = 7.8$. The inner scales are $(\pm x - d_4/2)d_3$ where + is for the cathode and − for the anode. The average pore velocities used are: 0, 0.43, 4.29, 10.7, 21.5, 32.2, and 42.9. The remaining parameters are $\alpha = 500$, $\gamma = 1$.

6.2. Relative pore width

The influence of the relative pore width ($\gamma = d_5/\lambda_D$) on the electrolyte advection performance increase is shown in the performance plots in Fig. 7. As the relative pore width increases the performance benefit from electrolyte advection disappears. This is most evident in Fig. 7c and d which compares the results for with (filled symbols) and without (open symbols) flow. This result is expected because the electrolyte advection effect relies on an ionic flux from the bulk flow in a region where the ion concentrations are not equal (i.e. where a net charge is present in the electrolyte). This causes a net ionic current to develop from an imbalance of ionic flux densities and an electrolyte potential gradient develops to maintain conservation of current as discussed previously. For cases where the width of the nano-pore is significantly greater than the Debye length (i.e. $\gamma \to \infty$), there is less overlap between the diffuse layers of the pore walls. The maximum cell current density (J_{cell}) also decreases as the relative pore width increases because the effective electrode surface area is less for larger width pores.

Fig. 8 shows cross pore distribution of the difference in ion concentrations taken at the pore midpoint for various values of the relative pore width. The disappearance of a net nonzero charge density across the pore is visible for the cases with larger values of γ at both the anode and cathode. The reduced nonzero charge density across the pore means that there is a less of an effect of the electrolyte advection on the net ionic current, and a reduced electrolyte potential gradient. It can be concluded from these results that in order for this electrode design to be

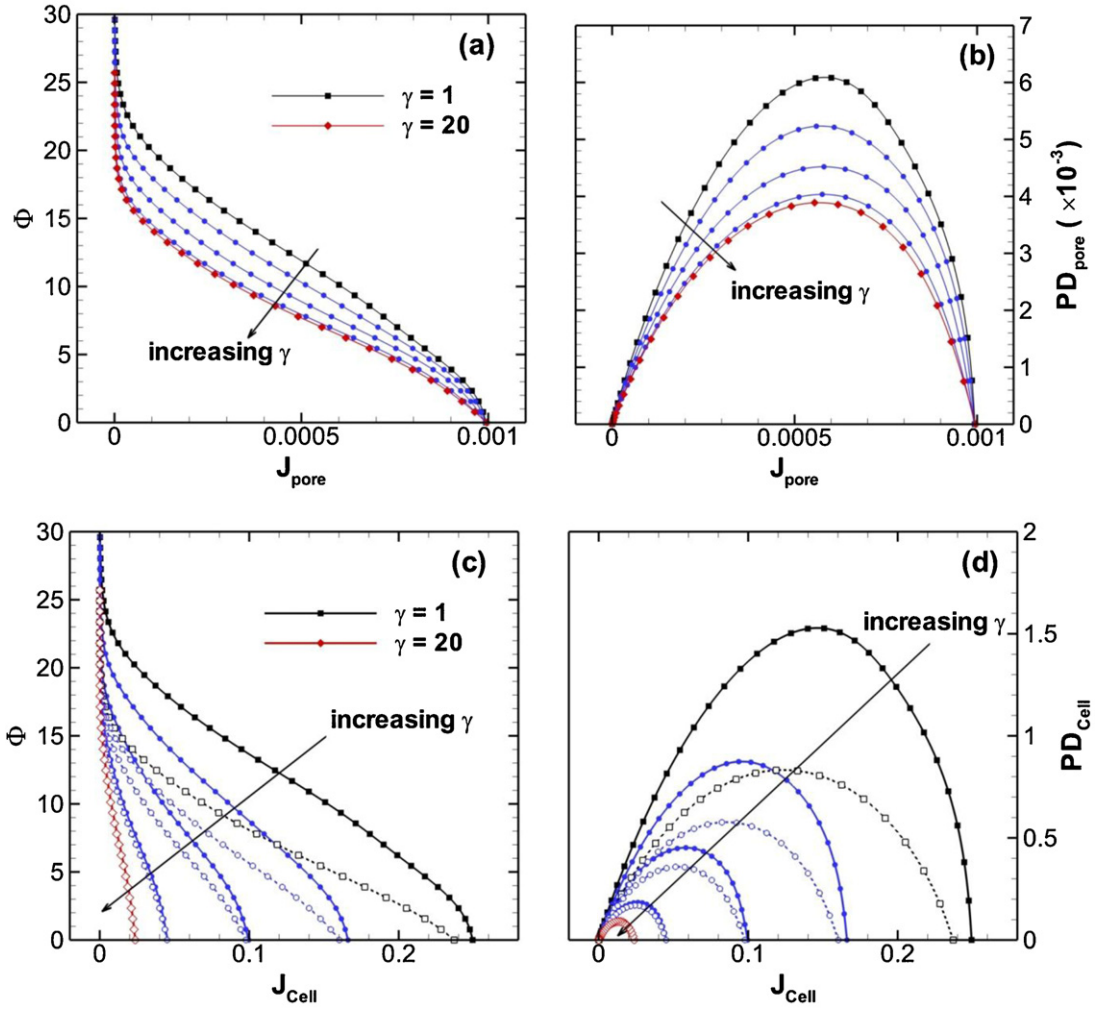

Fig. 7. Device performance for various relative pore widths, γ. Performance plots shown are (a) a *V–I* plot and (b) a power density plot for actual electrode surface area and (c) a *V–I* plot and (d) a power density plot for nominal electrode surface area. The relative pore widths used are: 1, 2, 4, 10, and 20. The remaining parameters are $\alpha = 500$, $\gamma = 1/(1+\gamma)$. The filled symbols are for $V_{Avg} = 42.9$ and the open symbols are for $V_{Avg} = 0$. Note: in (c) and (d), for $\gamma = 20$, the traces for the different velocities exactly overlap.

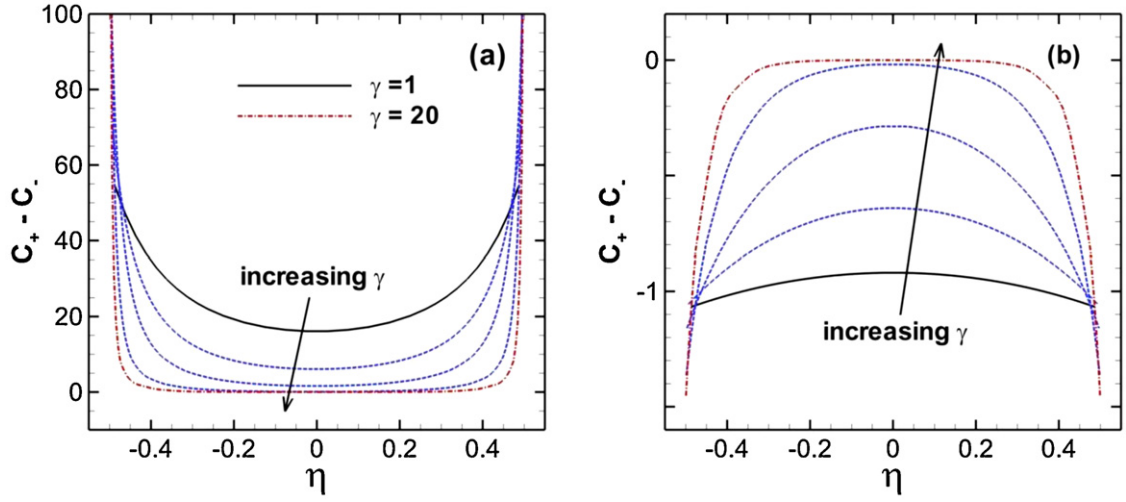

Fig. 8. Charge density distributions across pore for various relative pore widths, γ. The (a) anode and (b) cathode charge density distributions are taken at the pore midpoint ($\xi = 0.5$) and are shown for $\psi_{An} = 0$, $\psi_{Ca} = 7.8$. The results are presented against the rescaled *Y* coordinate, $\eta = Y/\in_D \gamma$. The relative pore widths used are: 1, 2, 4, 10, and 20. The remaining parameters are $\alpha = 500$, $\theta = \gamma/(1+\gamma)$, $V_{Avg} = 42.9$.

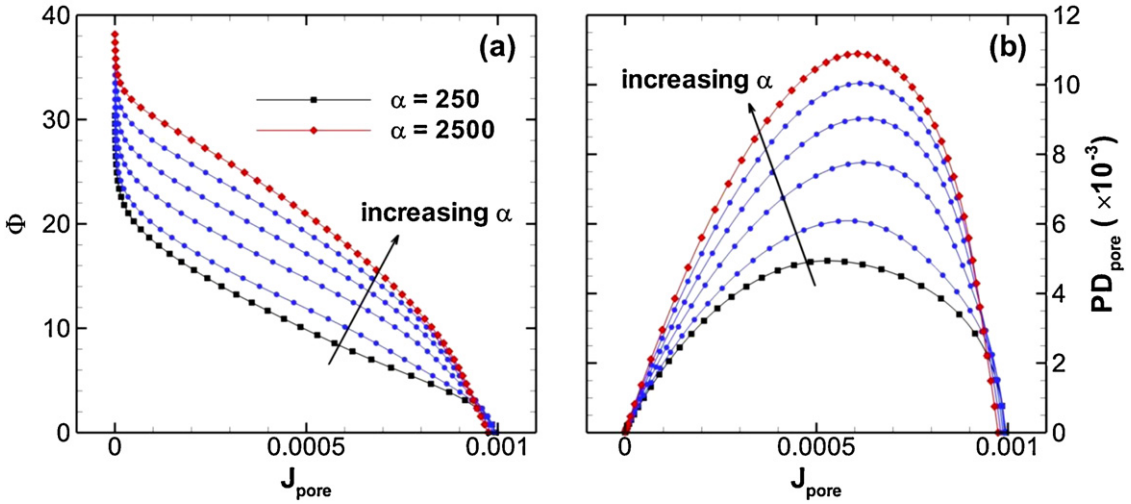

Fig. 9. Device performance for various pore relative lengths, α. Performance plots shown are (a) a *V–I* plot and (b) a power density plot for actual electrode surface area. The values of α shown are 250, 500, 1000, 1500, 2000, and 2500. The remaining parameters are $\gamma = 1$, $V_{Avg} = 42.9$.

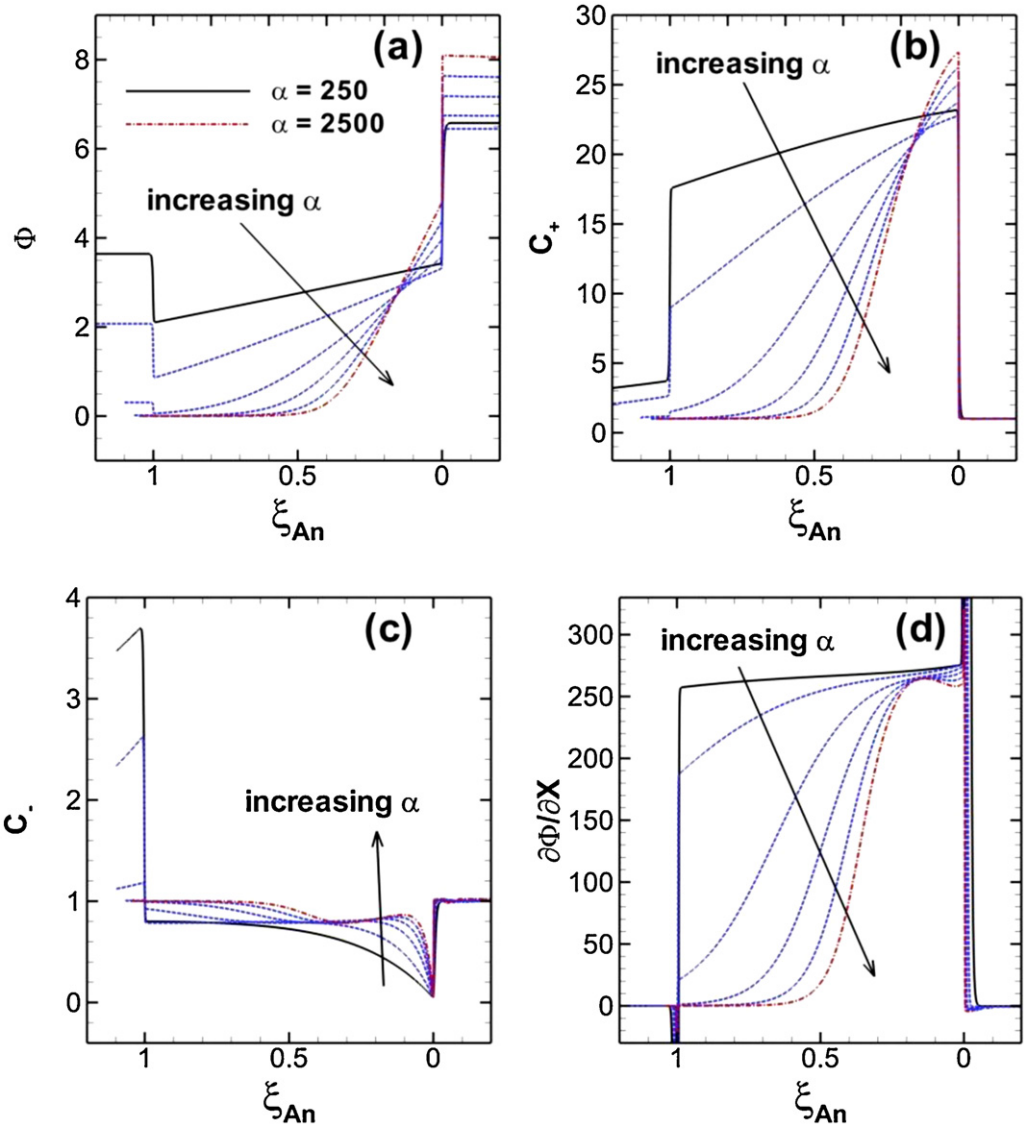

Fig. 10. Electrolyte potential and concentration distributions along an anodic pore for various pore relative lengths, α. The (a) electrolyte potential, (b) cation concentration, (c) anion concentration and (d) potential gradient distributions are taken along the pore centerline in the anode inner regions and are shown for $\psi_{An} = 0$, $\psi_{Ca} = 7.8$. The inner scale is $(-x - d_4/2)/d_3$. The values of α shown are 250, 500, 1000, 1500, 2000, and 2500. The remaining parameters are $\gamma = 1$, $V_{Avg} = 42.9$.

effective, the nano-pore widths must be on the order of the Debye length.

6.3. Relative pore length

How the pore relative length α influences the performance improvements from electrolyte advection through a nano-pore is presented in Fig. 9. Fig. 9b shows that the peak power density increases by a factor greater than 2.5 for a tenfold increase in pore relative length. This performance gain is the result of electrolyte distributions along the pore axis leading to an entrance region where the kinetics is not restricted by electric effects. The electrolyte potential and concentration distributions along the anode pore axis are shown in Fig. 10 for various pore relative lengths.

The distributions exhibit very interesting characteristics for the larger relative pore lengths. The electrolyte potential and cation concentration distributions begin to demonstrate very nonlinear behavior. The anion distribution was already nonlinear near the pore exit. Interestingly the exit distribution of anions is not a function of pore length, so the longer pores have a more significant upstream zone where the anion flux is dominated by advection.

The development of the nonlinear cation concentration distribution can be attributed to the requirement of charge balance between the EDL and the polarized electrode. Since the anion concentration is relatively fixed by the constant anion flux constraint, the difference of charge must be made up by excess cations. This creates an effective 'specified' total quantity of cations within the EDL (or nano-pore). As was mentioned before, a gradient in the electrolyte potential and cation concentration is present to balance the cation flux with the anion flux to maintain the conservation of current density; the number of excess cations exiting the anode pore cannot be greater than the number of cations released by the electrode kinetics.

The concentration and electrolyte potential gradients in the downstream section of the pore are largely determined by the advection flux of cations, and are therefore not significantly affected by pore length. Fig. 10d confirms that the potential gradients near the pore outlet are indeed very similar for all pore lengths, a fact that is important because it leads to the complex concentration and electrolyte potential distributions presented. The presence of the concentration gradient along with a specific total amount of cations in the nano-pore drives the concentration of cations back to the bulk value in the upstream section of the pore. As the cation and anion concentrations return to their bulk values, the electrolyte returns to a state of zero charge and the electrolyte potential returns to zero in this upstream zone. The electrode kinetics are, therefore, no longer limited by the electric field effects at the interface (which are no longer present) and are allowed to proceed at their spontaneous rates, leading to a higher kinetic rate. The critical pore length required for this upstream zone to occur is a function of electrode charge and electrolyte velocity. As alpha (α) increases even more, the device performance should continue to increase as well, but for values of alpha greater than 2500 the problem becomes too nonlinear and convergence of the numerical simulation becomes difficult.

7. Conclusions

In this work, a novel electrode design is presented in the context of a unique device configuration. The electrode design consists of a porous electrode with regularly spaced pores with a uniform pore structure. The electrolyte reactant streams are allowed to flow through their respective porous electrodes for merging in a center channel section where they are then sent out to waste. This electrode design and device configuration allows for improved performance through an advection effect on the diffuse region of the electric double layer. The nature of this advection affect is studied through electrolyte and reaction plane distributions. The device analysis is done by breaking the full device domain into 3 regions: typical anode periodic pore region, typical cathode periodic pore region, and the center channel section region. Each region is then analyzed using a 2-dimensional numerical simulation of the PNP-NS model equations with a g-FBV equation for electrode kinetics. Finally, the simulation was completed with a numerical algorithm capable of resolving all 3 regions into a single solution.

The device configuration presented with the regular nanoporous geometry was found to be able to increase the device performance in the presence of electrolyte advection. By neglecting the neutral species transport and normalizing current density with the actual electrode surface area, the presence of an electric double layer advection effect is revealed. This effect is shown to increase fuel cell performance with increasing flow rate. As the pore width increases to values significantly larger than the Debye length, the advection flux in the EDL is severely reduced, effectively eliminating this kinetic benefit. Additionally, in pores with a large relative pore length, the effect of the advection within the EDL causes very nonlinear behavior and the development of a zero charge region in the electrolyte in the upstream sections of the pore. This zero charge region allows the exothermic electrode reactions to proceed as fast as their spontaneous rates while still developing a potential difference across the cell. This means that a device operating with the performance benefit will have significantly reduced kinetic losses.

References

[1] A.A. Franco, P. Schott, C. Jallut, B. Maschke, A multi-scale dynamic mechanistic model for the transient analysis of PEFCs, Fuel Cells 7 (2007) 99.
[2] I. Sprague, D. Byun, P. Dutta, Effects of reactant crossover and electrode dimensions on the performance of a microfluidic based laminar flow fuel cell, Electrochimica Acta 55 (2010) 8579.
[3] I.B. Sprague, P. Dutta, Modeling of diffuse charge effects in a microfluidic based laminar flow fuel cell, Numerical Heat Transfer Part A – Applications 59 (2011) 1.
[4] P.M. Biesheuvel, M. van Soestbergen, M.Z. Bazant, Imposed currents in galvanic cells, Electrochimica Acta 54 (2009) 4857.
[5] I.B. Sprague, P. Dutta, Depth averaged analytic solution for a laminar flow fuel cell with electric double layer effects, SIAM Journal of Applied Mathematics 72 (4) (2012) 1149.
[6] I. Sprague, P. Dutta, Role of the diffuse layer in acidic and alkaline fuel cells, Electrochimica Acta 56 (2011) 4518.
[7] K. Aoki, Theory of the diffuse layer when a strong acid is reduced without supporting electrolyte, Journal of Electroanalytical Chemistry 488 (2000) 25.
[8] H. Sakaguchi, R. Baba, Theory of the diffuse layer when a strong acid is reduced without supporting electrolyte, Physical Review E 76 (2007) 011501.
[9] R. He, S.L. Chen, F. Yang, B.L. Wu, Dynamic diffuse double-layer model for the electrochemistry of nanometer-sized electrodes, Journal of Physical Chemistry B 110 (2006) 3262.
[10] J. Lim, J.D. Whitcomb, J.G. Boyd, J. Varghese, Effect of electrode pore geometry modeled using Nernst-Planck-Poisson-modified Stern layer model, Computational Mechanics 43 (2009) 461.
[11] D.B. Robinson, C.-A.M. Wu, B.W. Jacobs, Effect of salt depletion on charging dynamics in nanoporous electrodes, Journal of the Electrochemical Society 157 (2010) A912.
[12] T.A. Zangle, A. Mani, J.G. Santiago, Effects of constant voltage on time evolution of propagating concentration polarization, Analytical Chemistry 82 (2010) 3114.
[13] I. Rubinstein, B. Zaltzman, Dynamics of extended space charge in concentration polarization, Physical Review E 81 (2010) 061502.
[14] J.-Y. Jung, P. Joshi, L. Petrossian, T.J. Thornton, J.D. Posner, Electromigration current rectification in a cylindrical nanopore due to asymmetric concentration polarization, Analytical Chemistry 81 (2009) 3128.
[15] C. Kubeil, A. Bund, The role of nanopore geometry for the rectification of ionic currents, Journal of Physical Chemistry C 115 (2011) 7866.
[16] P.M. Biesheuvel, Y. Fu, M.Z. Bazant, Diffuse charge and Faradaic reactions in porous electrodes, Physical Review E 83 (2011) 061507.
[17] L. Permann, M. Latt, J. Leis, M. Arulepp, Electrical double layer characteristics of nanoporous carbon derived from titanium carbide, Electrochimica Acta 51 (2006) 1274.
[18] J. Varghese, H. Wang, L. Pilon, Simulating electric double layer capacitance of mesoporous electrodes with cylindrical pores, Journal of the Electrochemical Society 158 (2011) A1106.

[19] R.Y. Chein, K.Y. Tsai, L.Y. Yeh, Analysis of effect of electrolyte types on electrokinetic energy conversion in nanoscale capillaries, Electrophoresis 31 (2010) 535.
[20] R. Chein, C.C. Liao, H.J. Chen, Thermodynamic reversibility analysis of electrokinetic energy conversion in nanofluidic channels, Nanoscale and Microscale Thermophysical Engineering 14 (2010) 75.
[21] E.R. Choban, L.J. Markoski, A. Wieckowski, P.J.A. Kenis, Microfluidic fuel cell based on laminar flow, Journal of Power Sources 128 (2004) 54.
[22] E.R. Choban, J.S. Spendelow, L. Gancs, A. Wieckowski, P.J.A. Kenis, Membraneless laminar flow-based micro fuel cells operating in alkaline, acidic, and acidic/alkaline media, Electrochimica Acta 50 (2005) 5390.
[23] I. Sprague, P. Dutta, S. Ha, Characterization of a membraneless direct-methanol micro fuel cell, Proceedings of the Institution of Mechanical Engineers Part A-Journal of Power and Energy 223 (2009) 799.
[24] E. Kjeang, R. Michel, D.A. Harrington, N. Djilali, D. Sinton, A microfluidic fuel cell with flow-through porous electrodes, Journal of the American Chemical Society 130 (2008) 4000.